Electronic Supplementary Information

Correlating the Atomic Scale Structure with the Reaction Mechanism: Degradation of Iridium Oxides via Oxygen Evolution from the Lattice

Olga Kasian*[abc‡], Simon Geiger[b§‡], Tong Li[bd], Jan-Philipp Grote[b], Kevin Schweinar[b], Siyuan Zhang[b], Christina Scheu[b], Dierk Raabe[b], Serhiy Cherevko[e], Baptiste Gault*[bf] and Karl J.J. Mayrhofer*[beg]

[a]Helmholtz-Zentrum Berlin GmbH, Helmholtz-Institute Erlangen-Nürnberg, 14109 Berlin, Germany
[b]Max-Planck-Institut für Eisenforschung GmbH, 40237 Düsseldorf, Germany
[c]Department of Materials Science and Engineering, Friedrich-Alexander-Universität Erlangen-Nürnberg, 91058 Erlangen, Germany
[d]Institute for Materials & Zentrum für Grenzflächendominierte Höchstleistungswerkstoffe (ZGH), Ruhr-Universität Bochum, 44780 Bochum, Germany
[e]Helmholtz-Institute Erlangen-Nürnberg for Renewable Energy (IEK-11), Forschungszentrum Jülich GmbH, 91058 Erlangen, Germany
[f]Department of Materials, Royal School of Mines, Imperial College, Prince Consort Road, London, SW7 2BP, UK
[g]Department of Chemical and Biological Engineering, Friedrich-Alexander-Universität Erlangen-Nürnberg, 91058 Erlangen, Germany.
*Email: olga.kasian@helmholtz-berlin.de; k.mayrhofer@fz-juelich.de; b.gault@mpie.de
[§]Present address: Deutsches Zentrum für Luft- und Raumfahrt (DLR), Pfaffenwaldring 38-40, 70569 Stuttgart

[‡]These authors contributed equally to this work

Materials and methods

Experimental procedure

XPS measurements were carried out (Quantera II, Physical Electronics, Chanhassen, MN, USA) using a monochromatic Al Kα X-ray source (1486.6 eV) and operating at 15 kV and 25 W. The binding energy scale was referenced to the C 1s signal at 285.0 eV. Casa XPS software was used to analyze the experimentally obtained spectra. The spectra were fitted after subtraction of a Shirley background. In all fits, the peak separation and the peak area ratios between the Ir 4f7/2 and the Ir 4f5/2 components were kept constant and equaled 3 eV and 4:3, respectively.

A Doniach-Šunjic profile with an asymmetry parameter of 0.1 and a spectrum convolution width of 230 was used for the peak fittings. Detailed discussion of Ir XP spectra interpretation can be found in the literature.[1-3] The spectra were measured directly after the preparation of the electrodes. To minimize contact of the samples with air they were transferred in a desiccator from the preparation to XPS chamber.

Scanning transmission electron microscopy (STEM) experiment was carried out in a probe-corrected Titan Themis microscope operated at 300 kV.STEM images were formed by scanning a sub-Angstrom probe with a 24 mrad convergence semi-angle and 50 pA current, and recorded by an annular bright field (ABF) detector with collection semi-angles of 8 - 16 mrad . Electron energy loss spectroscopy (EELS) was acquired by the post-column energy filter Quantum ERS at 1 eV dispersion and 0.1 s/pixel. The Oxygen K-edge intensity map was integrated between 520 and 540 eV after subtracting the background from power law fitting.

Needle-shaped APT specimens were prepared by means of a site-specific lift-out procedure using a FEI Helios 600 Nanolab focused ion beam (FIB)/scanning electron microscope. A 200-nm thick protective Cr-layer was coated on top of Ir by electron-beam deposition in order to protect the surface oxides (Fig. S1a-b). The APT experiments were conducted on a CAMECA LEAP 5000 XS instrument equipped with an ultraviolet laser with a spot size of 2 µm and a wavelength of 355 nm. The detection efficiency of this state-of-the-art microscope is ~80%. Data was acquired in laser pulsing mode at a specimen temperature of 60 K, with a target evaporation rate of 5 ions per 1000 pulses, a pulsing rate of 200 kHz, laser pulse energy of 60 pJ. The APT data were reconstructed and analysed using the commercial IVAS 3.6.14™ software. The error bars for the concentration in this study have been calculated by $\sqrt{(c * (100 - c)/N}$, where c is the concentration (in at.%) and N is the total number atoms (*18*).

Secondary-Ion mass spectrometry measurements were performed using PHI NanoToF II time of flight mass spectrometer (Physical Electronics, Chanhassen, MN, USA). The samples were transferred from a desiccator to the intro chamber of the instrument, to avoid replacement of labeled atoms with air. The working pressure in the chamber during the measurements was 1.33 10^{-8} Pa. The instrument was operated with a $^{69}Ga^{+}$ primary ion source, having both the advantage of a small spot size and the enhancement of negative secondary ion yield. The high spatial resolution is achieved by coaxial primary and secondary ion optics, which also implies that primary and secondary species need to have opposite polarity. Therefore, negative secondary ions are extracted into the double focusing mass spectrometer, consisting of an electrostatic sector combined with a magnetic sector, this combination lead to an achromatic filtering according to mass-to-charge ratio. The oxygen (^{16}O = 15.9949 amu, ^{17}O = 16.9991 amu, ^{18}O = 17.9991 amu,) and secondary electron spectra were acquired in parallel as 256 × 256 pixel images with a dwell time of 5 ms per pixel and a probe current of 1 pA. The measurements were performed in conditions where there was no mass-interference between ^{18}O and $H_2{}^{16}O$ in the results. Considering that Ir oxides undergo reduction under experimental procedure, the obtained data cannot be quantified. This also results in low intensity of measured signals.

For stability measurements the prepared Ir oxide films served as the working electrodes in the scanning flow cell (SFC) coupled to an inductively coupled plasma mass spectrometer (ICP-MS, NexION 300X, Perkin Elmer) as described elsewhere.[4,5] The SFC is schematically shown in Figure S1a. All presented data are normalized to the geometric area of the working electrode (1×10^{-2} cm^2) assuming low roughness of the sputtered films. A graphite rod, placed in the inlet

channel of the SFC and saturated Ag/AgCl electrode were utilized as the counter and reference electrodes, respectively. All reported potentials are referenced to the reversible hydrogen electrode (RHE) potential, measured in each day of experiments using a polycrystalline platinum foil (99.99%, MaTeck, Germany) in hydrogen saturated 0.1 M $HClO_4$. After saturation with Ar, this solution was used in all electrochemical measurements. The ICP-MS was calibrated every day of experiment prior to the electrochemical measurements and the internal standard of 10 µg L^{-1} ^{187}Re was used.

The volatile oxygen products with mass to charge ratios of 32, 34 and 36 were measured using scanning flow cell – on-line electrochemical mass spectrometer (OLEMS) set up, previously described in.[6] In contrast to SFC connected to the ICP-MS, here the PTFE tip from the top of the cell through an extra vertical channel was introduced (Figure S1b). In this case, surface area of the working electrode was 12.5×10^{-2} cm^2. A 50 μm thick PTFE Gore-Tex membrane with a pore size of 20 nm, through which products can evaporate into the vacuum system of the mass spectrometer (Extrel, Pennsylvania, USA), was mounted onto the very end of the tip. The approximate distance from the tip to the electrode was about 30 μm, which is determined by the thickness of the silicon ring sealing around the cell opening and the applied contact force. These parameters affect the sensitivity and, therefore, they were kept constant during the whole set of measurements. The small size of pores and the thickness of the membrane result in the reduction of the water background pressure inside the vacuum and provide a good response time. Prior to measurements electrolyte was purged with Ar during 2 hours to ensure that no oxygen is coming from the air. Such optimized configuration results in good response time and high sensitivity. All OLEMS measurement were performed in electrolyte containing 0.1 M $HClO_4$ in ultrapure $H_2{}^{16}O$ water. A potentiostat (Gamry Reference 600, USA) was used for the electrochemical measurements with both setups. Each measurement was reproduced at least three times on three different samples prepared by the identical procedure.

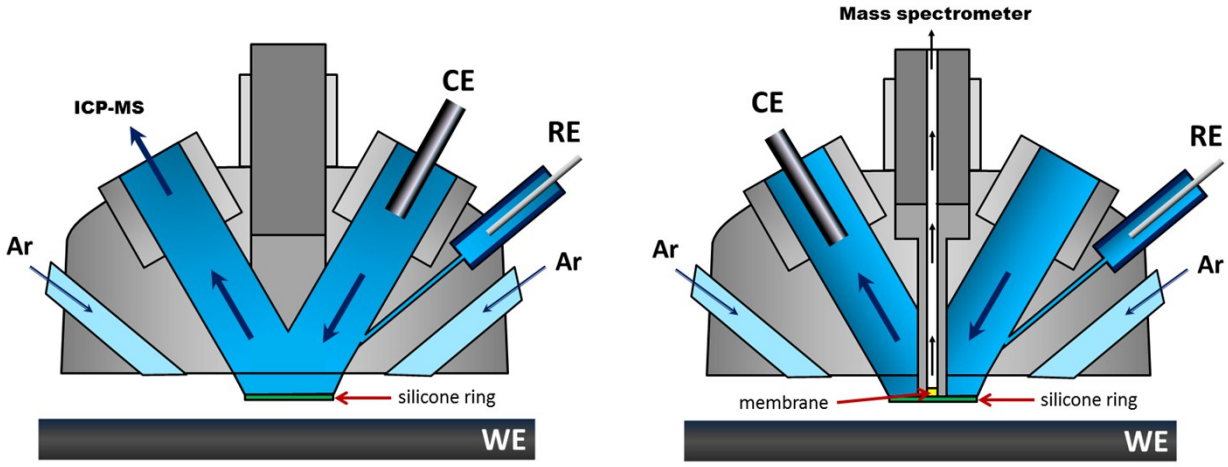

Figure S1. Schematic representation of SFC-ICP-MS and SFC-OLEMS setups.

Materials characterization

XPS characterization.

XPS data of reactively sputtered Ir oxide are presented in Fig. S2. The Ir $4f_{7/2}$ binding energy is 61.8 eV corresponding to IrO_2.[3,7] Detailed deconvolution of the Ir 4f spectra (Figure S2a) shows that Ir^{IV} is the only oxidation state of element in this sample, while spectra of O 1s level has significant contribution of lattice oxygen (529.9 eV) in reactively sputtered oxide (Figure S2b). Depth profiling with Ar up to 80 nm does not affect XP spectra, ensuring similarity of surface and bulk composition.

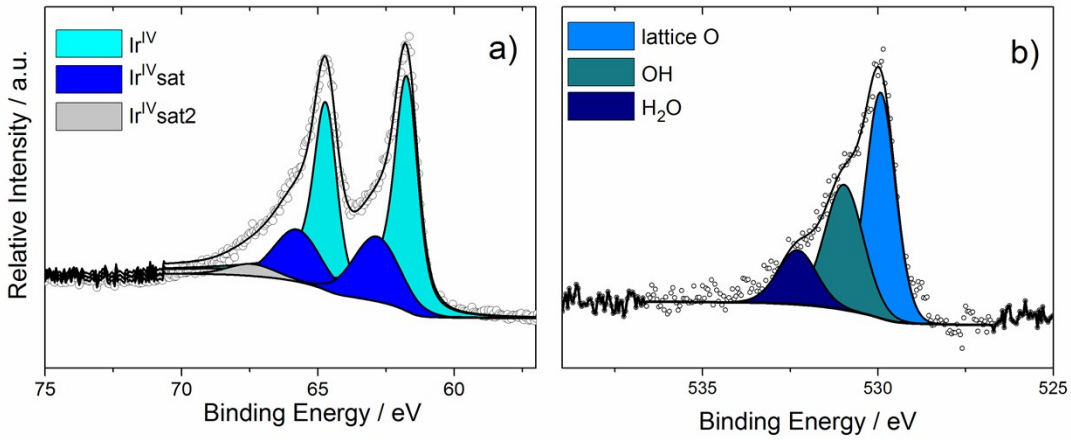

Figure S2. XP spectra of a) Ir 4f and b) O 1s levels obtained for reactively sputtered oxide.

In agreement with with literature data,[3] the spectrum of hydrous oxide shows contribution of Ir^{III} and Ir^{IV} in Ir 4f level (Fig. S3a). Considering spectrum of O1s level (Fig. S3b) hydrous oxide prepared as described above mainly consists of OH groups and low amount of lattice oxygen.

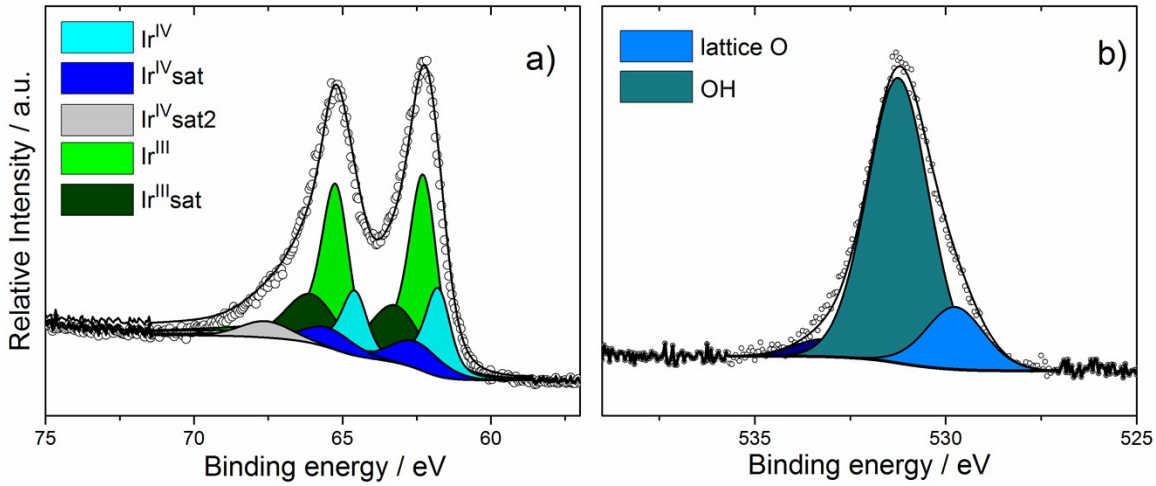

Fig. S3. XP spectra of a) Ir 4f and b) O 1s levels obtained for hydrous IrO_x.

Note that both samples were exposed to air prior to the XPS measurements, which results in presence of H2O species in the specta.

STEM analysis.

The porous morphology of hydrous oxide was confirmed by STEM-HAADF imaging (Fig. S4a). A complete coverage of the hydrous oxide on Ir is confirmed. The arrows indicate 2 areas with dark contrast, suggesting low mass density of materials there. It is also confirmed by EELS spectrum imaging that such areas have less Ir and O, as shown in Fig. S4b-c. . The size of the low mass density areas, ~5 nm, corresponds to the pores features in APT data between the outer oxide layer and the Ir bulk (Fig.1c,d) . In addition, thicknesses of different layers were measured by STEM to serve as a benchmark in the APT reconstruction.

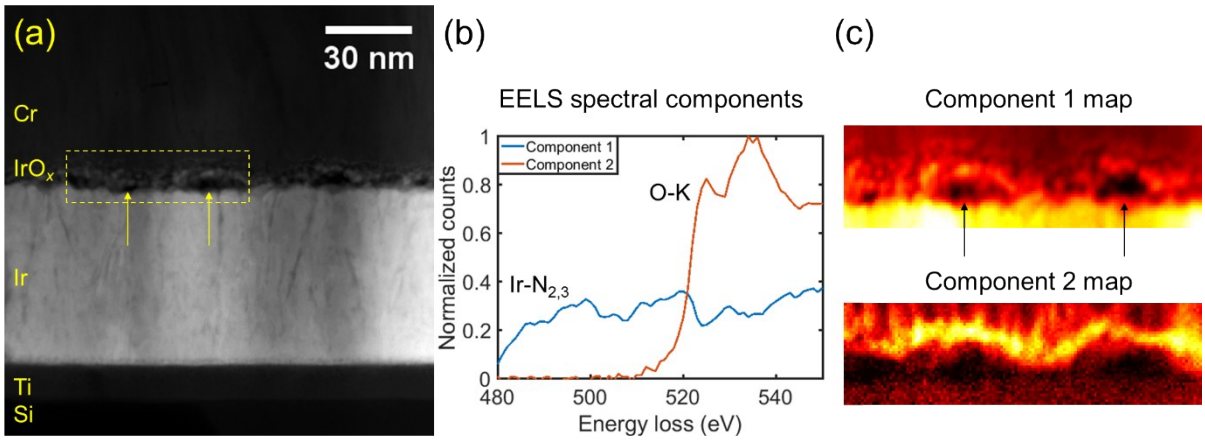

Fig. S4. (a) STEM-HAADF image of the thin films from bottom to top: Si wafer, 5 nm Ti, 80 nm Ir (including its hydrous oxide), and 200 nm Cr as a protective layer. The dashed box indicates the area of EELS spectrum imaging. (b) Spectral components from EELS spectrum imaging of Ir-$N_{2,3}$ and O-K signals and (c) their corresponding spatial distribution maps.

APT specimen preparation of hydrous oxide

Two different approaches were employed to prepare APT samples, because it is difficult to achieve APT data of the hydrous oxide after detection of the outer oxide in Fig. S6.

Fig. S5a shows a SEM image of a representative needle-shaped APT sample with Cr capping on the top, followed by Ir oxide and Ir (brighter contrast), and Si substrate at the bottom. The APT samples of data shown in Figure 1f-i and Fig. S6, were prepared from this method.

The SEM image in Fig. S5b shows an unsharpened APT sample prepared by a vertical lift-out method, namely Ir oxide layer was positioned vertically. An annular milling procedure was proceeded to position the center of the tip at the Cr/Ir interface, as delineated by the white dashed line. The APT data in Figure 1a-e were prepared by the vertical lift-out method.

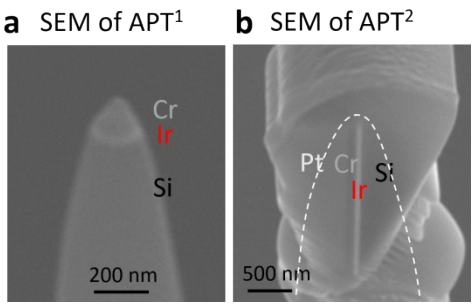

Fig. S5. SEM images of APT sample prepared by two FIB lift-out methods.

APT data on hydrous oxide

The top-down and side views of 3D APT reconstruction of the outer layer of hydrous oxide are shown in Supplementary Figures 6a and 6b, respectively.

The mass spectra of both, the outer oxide and the porous oxide treated in the deuterated tracer electrolyte (Fig. S7a, d) shows the existence of molecular ion at 18 Da. The molecular ion at 18 Da could be OD+ or OH2+ where H stems from the vacuum chamber. The absence of OH+ at 17 Da excludes the co-evaporation of oxygen with hydrogen from the vacuum chamber. Furthermore, in both outer oxide and porous oxide, IrO2+ molecular ion was detected (Fig. S7c, f). In comparison, the detection of peak at 17 Da (OH+) of the outer oxide (Fig. S7b) prepared by HClO4 and H2O is consistent with the observation revealed in Fig. S7a although hydrogen could be partly from the vacuum. Additionally, some of the porous oxide regions contain Cl2+ from the electrolyte in both, deuterated and normal samples (Fig. S7e).

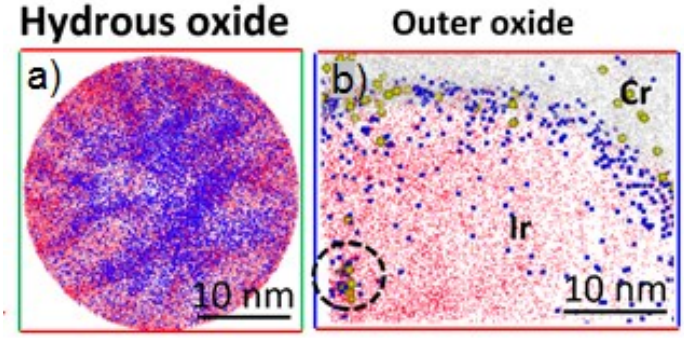

Fig. S6. (a) the top-down and (b) side views of 3D APT reconstruction for outer layer of hydrous oxide.

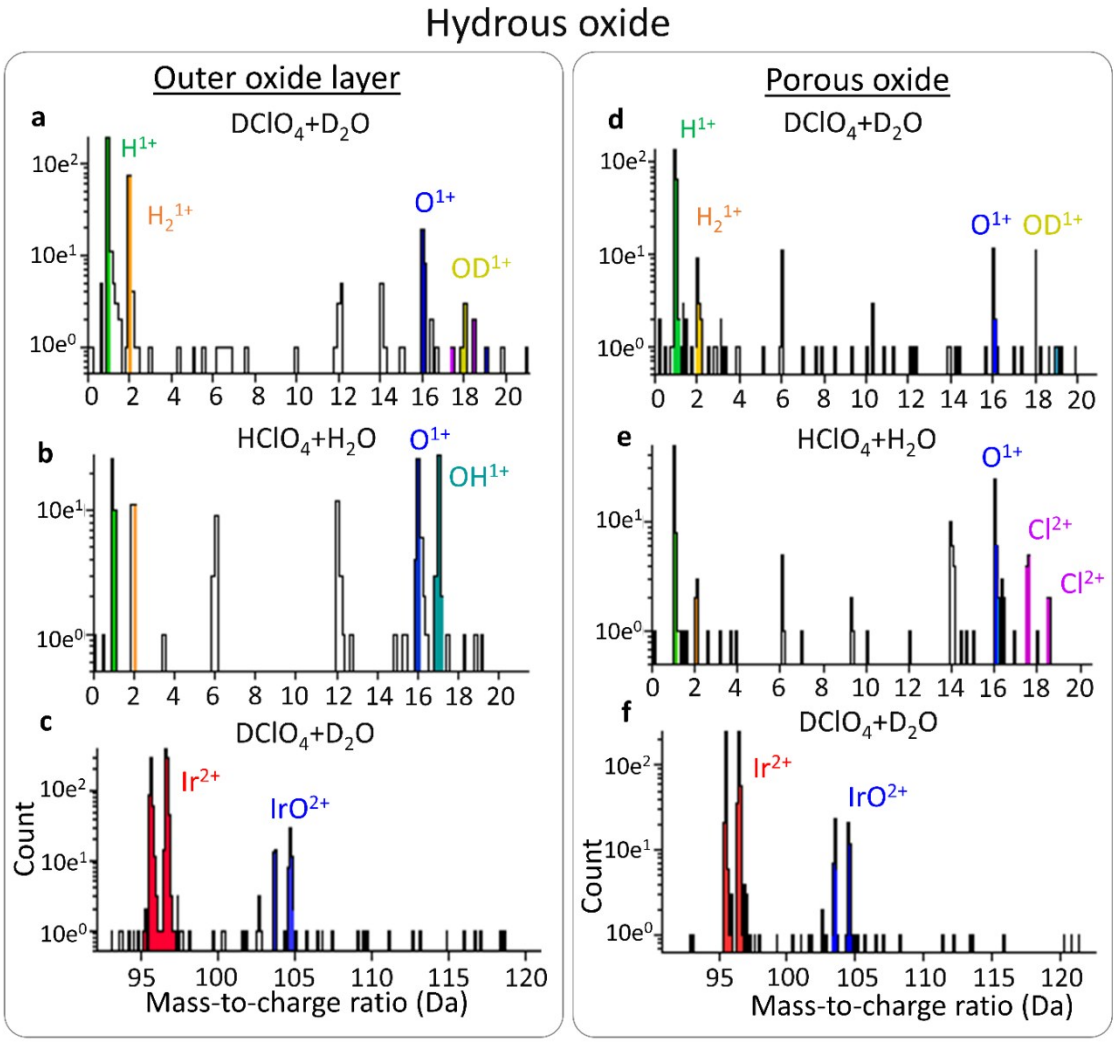

Fig. S7. Mass spectrum of outer layer of hydrous oxide (a-c), and porous oxide (d-f) treated in $DClO_4$ and D_2O and $HClO_4$ and H_2O respectively.

ToF-SIMS analysis of the ^{18}O labeled oxides

ToF-SIM spectra for ^{18}O-labelled hydrous $Ir^{18}O_x$ and reactively sputtered $Ir^{18}O_2$ are shown in Fig. S8a and Fig. S8b, respectively. For both materials ^{18}O-containing ions dominate in the spectra.

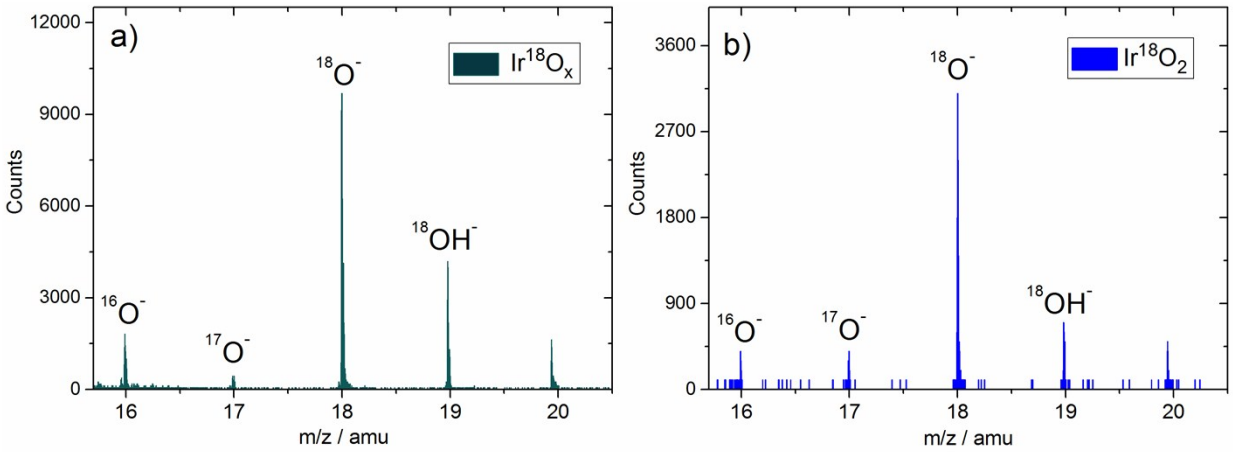

Fig. S8. SI mass spectra of hydrous $Ir^{18}O_x$ (a) and reactively sputtered $Ir^{18}O_2$ (b). Both samples were exposed to air during the transfer to ToF SIMS cahmber.

Results

Removal of ^{18}O-water residuals from the pores of hydrous oxide.

When present in pores of the sample of hydrous oxide water-^{18}O can lead to higher amount of detected mass to charge ratios 34 and 36. Therefore, after preparation of hydrous oxide by the CV experiments the electrodes were ultrasonically threated in ultrapure water-^{16}O. Then the samples were transferred to the high vacuum PVD chamber and annealed at 100 C in vacuum during the 2 hours at 10^{-8} mBar. The following conditions were chosen based on the change of OLEMS signals for species with m/z=34 and m/z=36. In details, Figure S9 shows OLEMS data obtained on ^{18}O-labelled hydrous oxide samples in as prepared state and after pre-treatment at 50 C, 100 C or 150 C.

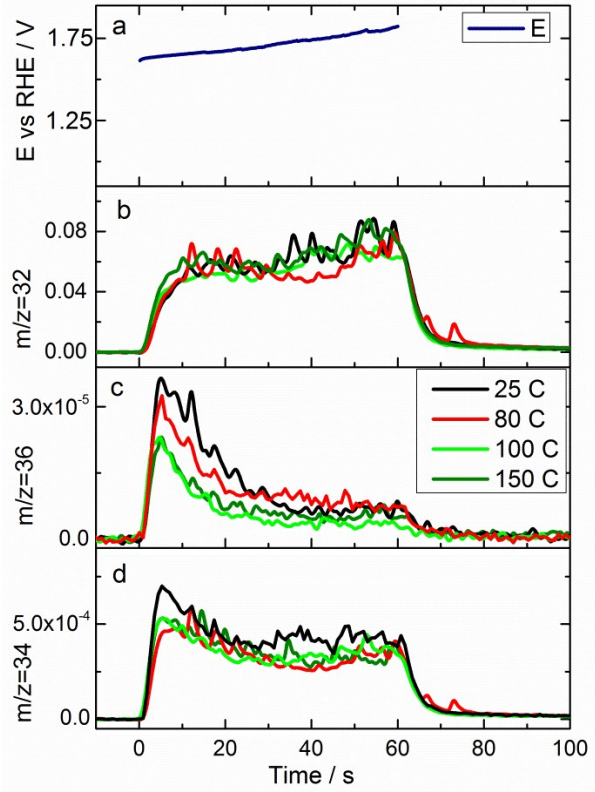

Fig. S9. Effect of thermal treatment of ^{18}O labelled hydrous oxide $Ir^{18}O_x$ in vacuum on the formation of $^{18}O^{16}O$ and $^{18}O^{18}O$ during the OER.

Thermal treatment in vacuum at 50 C leads to slight decrease in a signal from m/z=34 compared to an as prepared sample (Figure 4d). The decrease in signal from m/z=36 with increasing up to 100 C temperature of treatment was observed. Apparently, during the thermal treatment at 100 C the physiosorbed water evaporates from the pores of the hydrous oxide. As a result of such treatment intensity of m/z=34 and m/z=36 corresponds to formation of oxygen from ^{18}O atoms of the oxide lattice. Since heat treatment at 100 C is sufficient for removal of water from the pores of hydrous oxide further increase of temperature to 150 C has no impact on the measured intensity of corresponding masses in OLEMS setup. Therefore thermal treatment of the samples at 100 C was chosen to prepare ^{18}O-labelled samples of hydrous oxide for the investigations reported in the manuscript.

Oxygen evolution products formed during anodic polarization of labeled hydrous $Ir^{18}O_x$

Fig. S10 shows profiles of formation of volatile products with mass to charge ratios of 32 ($^{16}O^{16}O$), 34 ($^{16}O^{18}O$ or $^{17}O^{17}O$) and 36 ($^{18}O^{18}O$) recorded during anodic polarization of labeled hydrous $Ir^{18}O_x$. First, potential was swept into anodic direction with a scan rate of 10 m Vs^{-1} till current density approached value of 20 mA cm^{-2} (Fig. S10a), then electrode was polarized at 15 mA cm^{-2} during 60 s (Fig. S10b) and identical anodic sweep of potential was performed again (Fig. S10c). In order to exclude the effect of isotope abundance in electrochemical measurements on labeled samples, the $^{16}O^{18}O$ and $^{18}O^{18}O$ signals were always measured for unlabeled samples and subtracted from those measured for ^{18}O-labeled samples. The data after subtraction are shown in Figure 2.

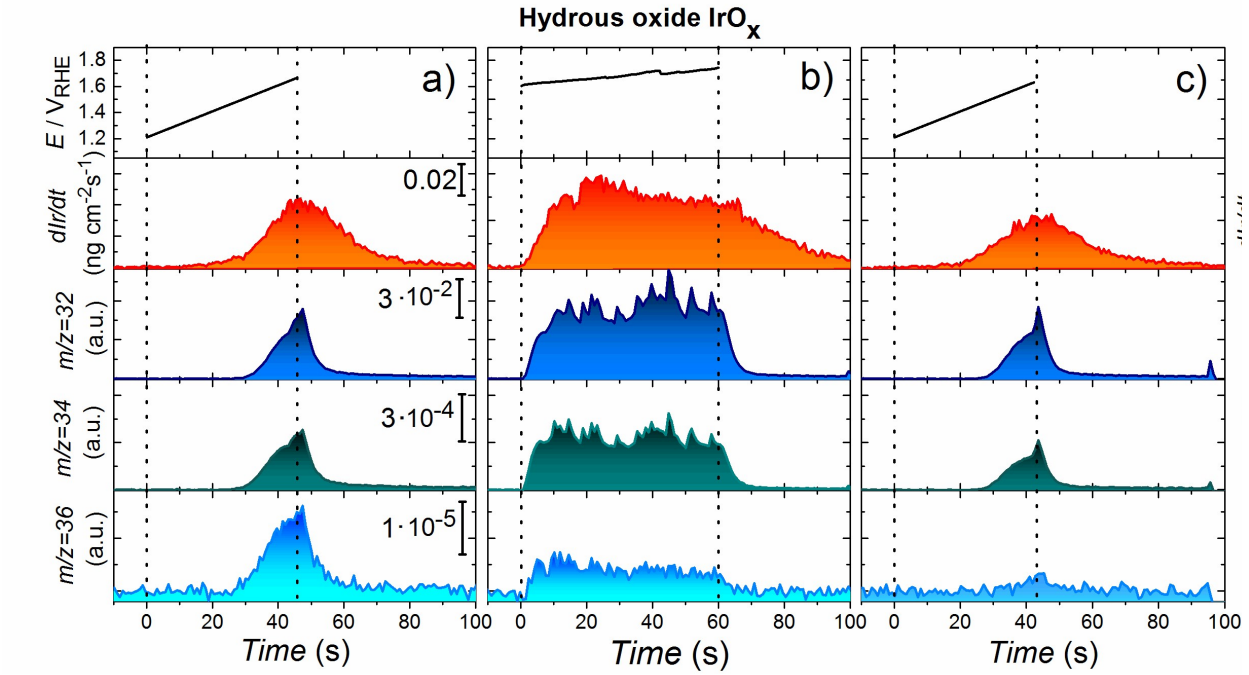

Fig. S10. On-line observation of lattice oxygen evolution and dissolution of hydrous $Ir^{18}O_x$ (a-c) and reactively sputtered $Ir^{18}O_2$ (d) during OER in 0.1 M $HClO_4$ in $H_2{}^{16}O$. The data are shown as it was received from the instrument. Applied (a, c) or measured (b) potential for the investigation of OER and corresponding Ir concentration profiles, $^{16}O^{16}O$, $^{16}O^{18}O$ and $^{18}O^{18}O$ signals plotted vs. time for an isotope labeled hydrous $Ir^{18}O_x$ electrode. Potential scans in (a) and (c) were performed from 1.2 V_{RHE} till current density reached 20 mA cm^{-2} with the scan rate of 10 mV s^{-1}. (b) Galvanostatic anodic polarization at 15 mA cm^{-2} during 60 s. The data is plotted as received during the measurements.

Oxygen evolution products formed during anodic polarization of unlabeled hydrous $Ir^{16}O_x$

Fig. S11 shows profiles of formation of volatile products with mass to charge ratios of 32 ($^{16}O^{16}O$), 34 ($^{16}O^{18}O$ or $^{17}O^{17}O$) and 36 ($^{18}O^{18}O$) recorded during anodic polarization of unlabeled hydrous $Ir^{16}O_x$. Similarly to the protocol employed to labeled electrode: first, potential was swept into anodic direction with a scan rate of 10 m Vs^{-1} till current density approached value of 20 mA cm^{-2} (Fig. S11a), then electrode was polarized at 15 mA cm^{-2} during 60 s (Fig. S11b) and identical anodic sweep of potential was performed again (Fig. S11c). The measured intensities of m/z 34 and 36 correspond to normal abundance of ^{17}O and ^{18}O isotopes in water. In order to exclude their effect in electrochemical measurements on labeled samples, these signals were always measured for unlabeled samples and subtracted from those measured for ^{18}O-labeled samples.

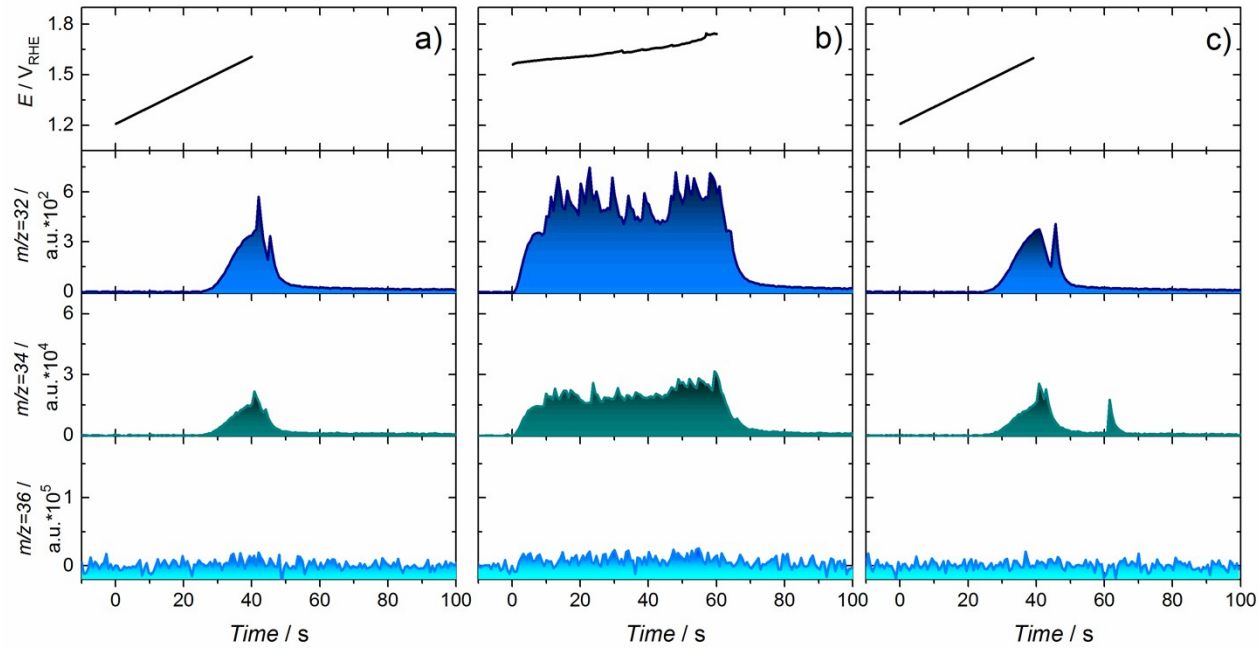

Fig. S11. On-line observation of oxygen evolution on unlabeled hydrous $Ir^{16}O_x$. The applied (a, c) or measured (b) potential for the investigation of OER and corresponding signals from $^{16}O^{16}O$, $^{16}O^{18}O$ and $^{18}O^{18}O$ plotted vs. time. Potential scans (a, c) were performed from 1.2 V_{RHE} to 20 mA cm^{-2} with the scan rate 10 mV s^{-1}; galvanostatic anodic polarization at 15 mA cm^{-2} during 60 s (b). Electrolyte 0.1 M $HClO_4$ in $H_2{}^{16}O$.

Oxygen evolution products formed on labeled hydrous $Ir^{18}O_x$ (a) and unlabeled hydrous $Ir^{16}O_x$

Profiles of formation of volatile products with m/z of 32, 34 and 36 measured during 180 s of anodic polarization at 15mA cm^{-2} of labelled $Ir^{18}O_x$ (a) and unlabeled $Ir^{16}O_x$ (b) hydrous oxide electrodes are shown in Fig. S12. Constant gradual decay of m/z 36 intensity is observed for ^{18}O-labelled sample, indicating constant exchange between oxygen atoms in lattice and those from water.

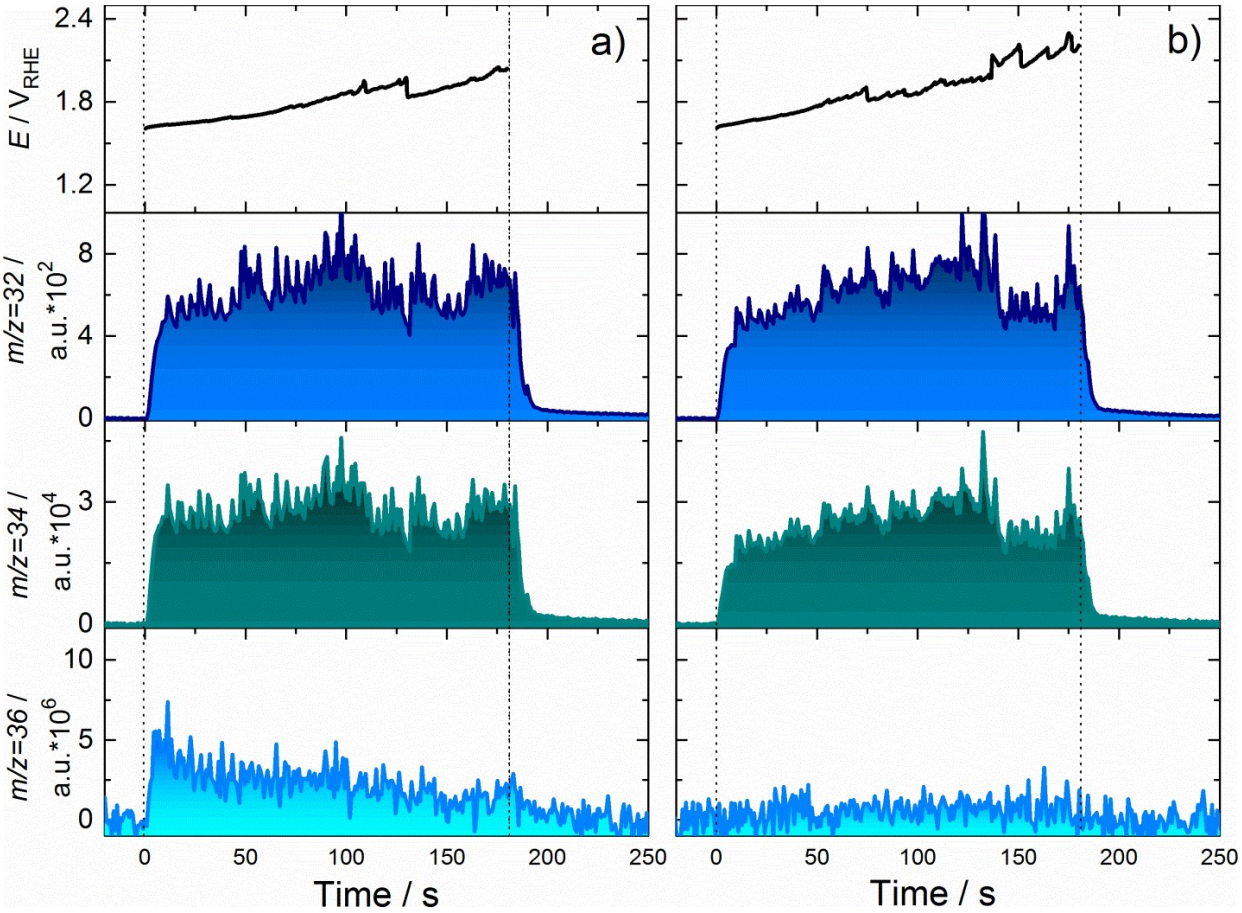

Fig. S12. Oxygen evolution on labeled hydrous $\mathbf{Ir^{18}O_x}$ (a) and unlabeled hydrous $\mathbf{Ir^{16}O_x}$ (b) oxides during 180 s of anodic polarization at 15 mA cm^{-2}. Electrolyte 0.1 M $HClO_4$ in $H_2{}^{16}O$. Prior to these measurements both electrodes were pretreated at 15 mA cm^{-2} during 60 s.

Formation of oxygen products on labelled $Ir^{18}O_2$ and unlabeled $Ir^{16}O_2$

Fig. S13 shows corresponding profiles of formation of volatile products with m/z of 32, 34 and 36 measured during anodic polarization at 25mA cm^{-2} of labelled $Ir^{18}O_2$ (a) and unlabeled $Ir^{16}O_2$ (b) prepared by reactive sputtering. Slightly higher formation of m/z of 36 is observed for ^{18}O-labelled sample, resulting from the lattice oxygen participation.

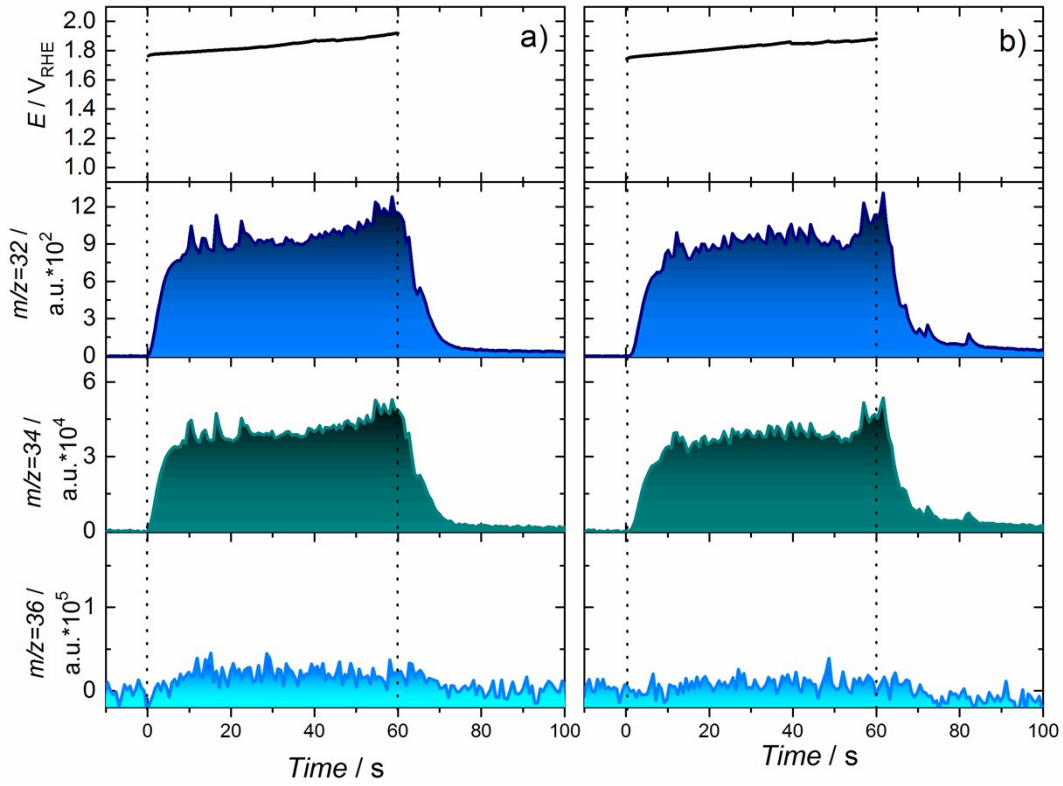

Fig. S13. Oxygen evolution on reactively sputtered labeled $\mathbf{Ir^{18}O_2}$ (a) and unlabeled $\mathbf{Ir^{16}O_2}$ (b) during 60 s of anodic polarization at 25 mA cm^{-2}. Electrolyte 0.1 M $HClO_4$ in $H_2{}^{16}O$.

Effect of applied current density on formation of volatile oxygen products on labelled $Ir^{18}O_x$.

Fig. S14 shows profiles of formation of volatile oxygen products with m/z of 32, 34 and 36 measured for labelled $Ir^{18}O_x$ during 60 s of anodic polarization at different current densities. Simultaneously measured Ir dissolution profiles are shown in Fig. S15.

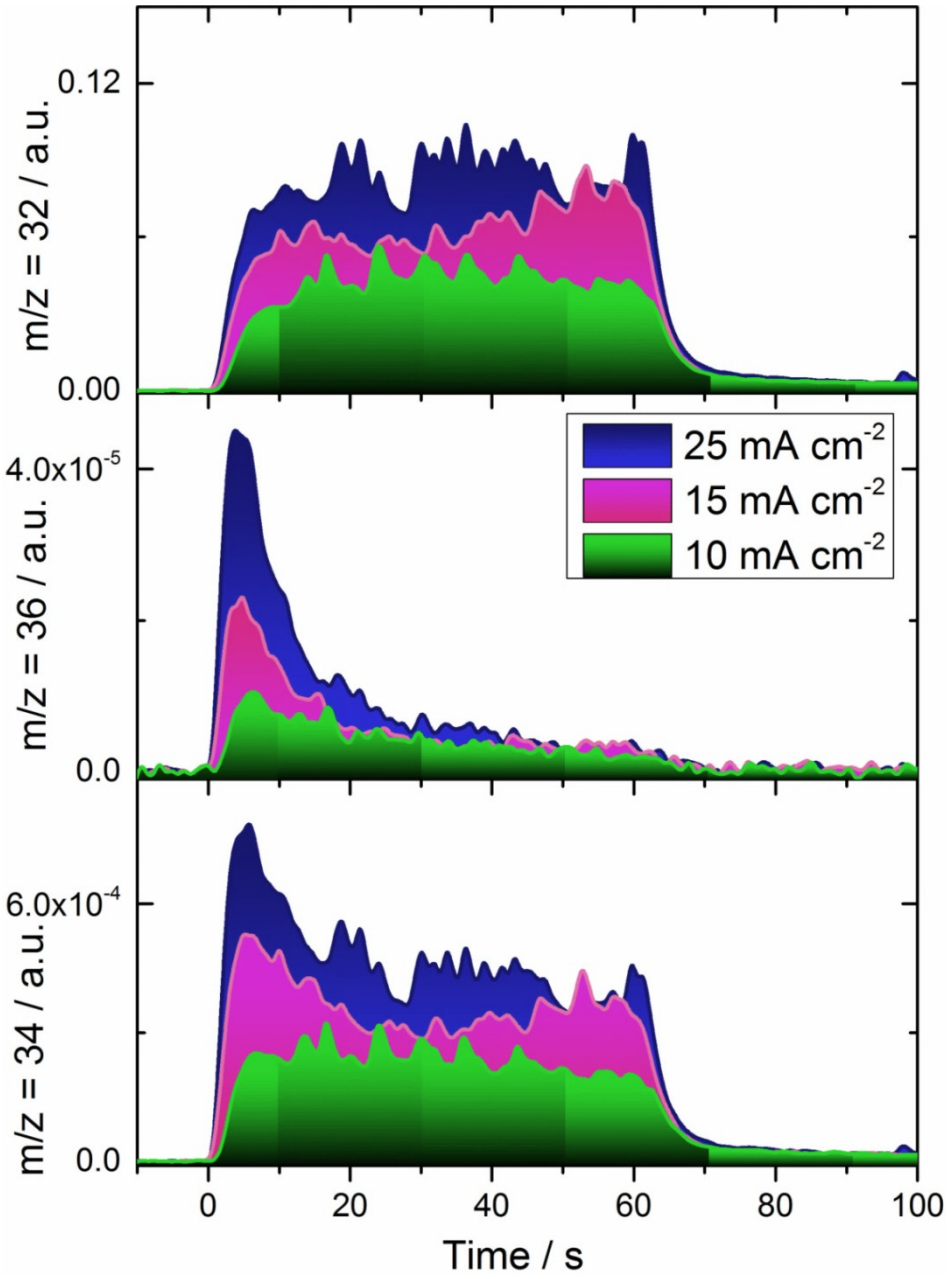

Fig. S14. Formation of volatile oxygen products with m/z of 32, 34 and 36 measured for labelled $Ir^{18}O_x$ electrode during 60 s of anodic polarization at 10, 15 and 25 mA cm^{-2}.

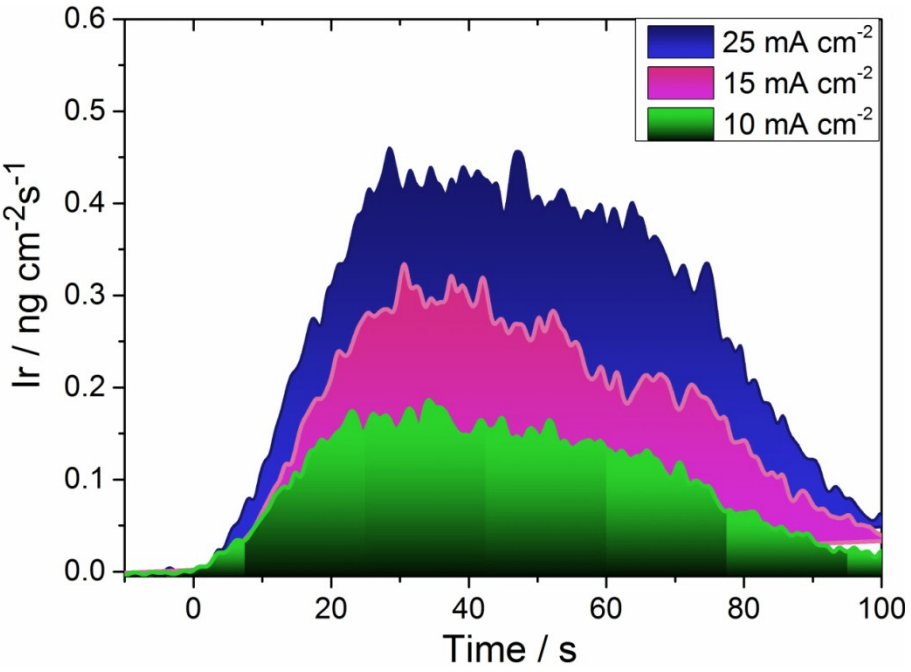

Fig. S15. Dissolution profiles recorded during 60 s of anodic polarization of hydrous IrOx at during 60 s of anodic polarization at 10, 15 and 25 mA cm^{-2}.

Relevance to the OER mechanism

The degradation mechanism depends on the nature of electrode and on the applied electrochemical conditions. The degradation occurs via formation of IrO_3 species in case of Ir oxides with low reactivity towards the OER. In this case in conditions of constant current polarization the value of potential at the electrode will be high enough to drive oxidation of Ir to the oxidation state Ir(VI). This mechanism of degradation was observed for thermally prepared IrO_2, which has low reactivity. In contrast both reactively sputtered IrO_2 and electrochemically prepared hydrous IrO_x exhibit high electrocatalytic activity towards OER as shown in Fig. S16.

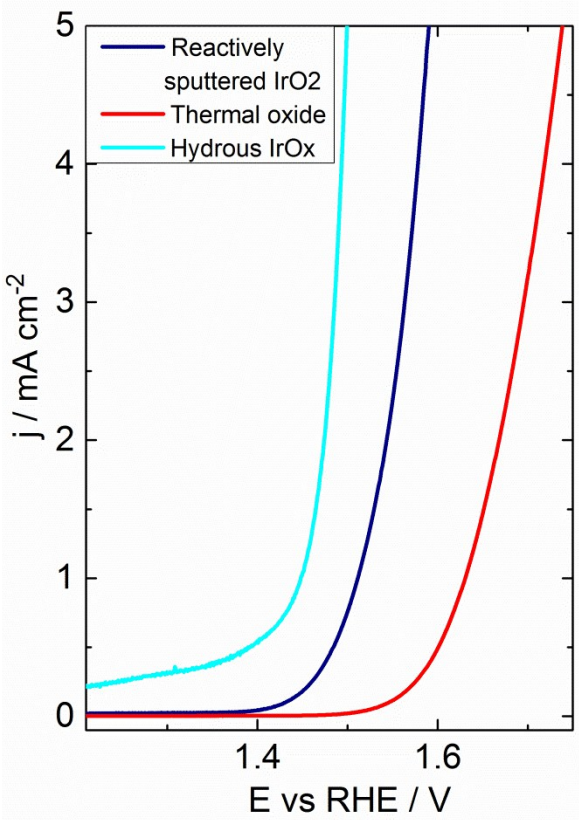

Fig. S16. Anodic quasi steady state polarization curves recorded on hydrous IrO_x (cyan), reactively sputtered IrO_2 (blue) and thermally prepared IrO_2 (red) recorded in 0.1 M $HClO_4$ with a scan rate 10 mV/s.

Approach to estimate the contribution of $^{16}O^{16}O$, $^{16}O^{18}O$ and $^{18}O^{18}O$ in OER on labelled hydrous oxide

Estimation of the contribution of each of the measured products in a total applied current was performed considering that OER and dissolution of Ir are the only anodic processes and assuming that dissolution of Ir is electrochemical process. Then the total applied current is

$I_{total} = I_{diss} + I_{O_2}$, where

I_{total} – total current applied to the electrode,

I_{diss} – partial current of Ir dissolution, estimated from the ICP-MS data using Faraday's law

$$I_{diss} = \frac{m_{Ir} z F}{M t}$$

m_{Ir} – mass of dissolved Ir, measured by ICP-MS,

z – number of electrons in reaction of Ir dissolution,

F – Faraday's constant,

t – duration of galvanostatic polarization,

M – molar mass of Ir.

I_{O_2} – partial current of oxygen evolution, calculated using the total applied current and I_{diss} current and equals (^{17}O contribution is neglegted as the natural abundance is ^{17}O is one magnitude smaller than the one of ^{18}O)

$I_{O_2} = I_{16_O16_O} + I_{16_O18_O} + I_{18_O18_O}$, where

$I_{16_O16_O}$ – partial current of oxygen evolution formed without participation of lattice oxygen atoms,

$I_{18_O18_O}$ – partial current of oxygen evolution formed of lattice oxygen atoms only

$I_{16_O18_O}$ – partial current of oxygen evolution formed by combination of water oxygen with lattice oxygen atoms.

Considering that ^{16}O^{16}O, ^{16}O^{18}O and ^{18}O^{18}O are the only formed oxygen molecules and give in total 100% of all oxygen

$$1 = \frac{A_{16_O16_O}}{A_{16_O16_O} + A_{16_O18_O} + A_{18_O18_O}} + \frac{A_{16_O18_O}}{A_{16_O16_O} + A_{16_O18_O} + A_{18_O18_O}} + \frac{A_{18_O}}{A_{16_O16_O} + A_{16_O}}$$

, where

$\frac{A_{16_O16_O}}{A_{16_O16_O} + A_{16_O18_O} + A_{18_O18_O}}$ - fraction of ^{16}O^{16}O molecules in the whole formed oxygen,

$\frac{A_{16_O18_O}}{A_{16_O16_O} + A_{16_O18_O} + A_{18_O18_O}}$ - fraction of ^{16}O^{18}O molecules in the whole formed oxygen,

$\frac{A_{18_O18_O}}{A_{16_O16_O} + A_{16_O18_O} + A_{18_O18_O}}$ - fraction of ^{18}O^{18}O molecules in the whole formed oxygen,

$A_{16_O16_O}, A_{16_O18_O}, A_{18_O18_O}$ – values obtained by integration of corresponding peaks in profiles measured by OLEMS. To obtain the contribution of the oxygen that is coming from the lattice to the partial currents and the total current respectively, the contribution of the natural abundance of ^{18}O needs to be taken into account and substracted. Therefore values of $A_{16_O18_O}, A_{18_O18_O}$ obtained after the substraction of a background. The corresponding signal measured in identical experimants performed on unlebelled samples is considered as a background.

Then, partial currents of $^{16}O^{16}O$, $^{16}O^{18}O$ and $^{18}O^{18}O$ equal, respectively

$$I_{16_O16_O} = \frac{A_{16_O16_O}}{A_{16_O16_O} + A_{16_O18_O} + A_{18_O18_O}} I_{O_2},$$

$$I_{16_O18_O} = \frac{A_{16_O18_O}}{A_{16_O16_O} + A_{16_O18_O} + A_{18_O18_O}} I_{O_2},$$

$$I_{18_O18_O} = \frac{A_{18_O18_O}}{A_{16_O16_O} + A_{16_O18_O} + A_{18_O18_O}} I_{O_2},$$

References

1 Freakley, S. J., Ruiz-Esquius, J. & Morgan, D. J. The X-ray photoelectron spectra of Ir, IrO2 and IrCl3 revisited. *Surface and Interface Analysis*, doi:10.1002/sia.6225 (2017).

2 Pfeifer, V. *et al.* The electronic structure of iridium and its oxides. *Surface and Interface Analysis* **48**, 261-273, doi:10.1002/sia.5895 (2016).

3 Pfeifer, V. *et al.* The electronic structure of iridium oxide electrodes active in water splitting. *Physical Chemistry Chemical Physics* **18**, 2292-2296, doi:10.1039/C5CP06997A (2016).

4 Cherevko, S., Geiger, S., Kasian, O., Mingers, A. & Mayrhofer, K. J. J. Oxygen evolution activity and stability of iridium in acidic media. Part 1. – Metallic iridium. *Journal of Electroanalytical Chemistry* **773**, 69-78, doi:http://dx.doi.org/10.1016/j.jelechem.2016.04.033 (2016).

5 Topalov, A. A., Katsounaros, I., Meier, J. C., Klemm, S. O. & Mayrhofer, K. J. Development and integration of a LabVIEW-based modular architecture for automated execution of electrochemical catalyst testing. *The Review of scientific instruments* **82**, 114103, doi:10.1063/1.3660814 (2011).

6 Grote, J.-P., Zeradjanin, A. R., Cherevko, S. & Mayrhofer, K. J. J. Coupling of a scanning flow cell with online electrochemical mass spectrometry for screening of reaction selectivity. *Review of Scientific Instruments* **85**, 104101, doi:10.1063/1.4896755 (2014).

7 Kasian, O. *et al.* On the Origin of the Improved Ruthenium Stability in RuO2–IrO2 Mixed Oxides. *Journal of The Electrochemical Society* **163**, F3099-F3104, doi:10.1149/2.0131611jes (2016).